

Simulations of Field Errors in IR magnets of a Muon Collider using MAD-X and COSY codes¹.

Valery Kapin and Yuri Alexahin

APC, Fermilab, P.O. Box500, Batavia 60510, IL

May, 2012

Abstract

In order to achieve peak luminosity of a Muon Collider (MC) in the $10^{35} \text{ cm}^{-2} \text{ s}^{-1}$ range very small values of beta-function at the interaction point (IP) are necessary ($\beta_{\text{IP}} \leq 1 \text{ cm}$) while the distance from IP to the first quadrupole can not be made shorter than $\sim 6 \text{ m}$ as dictated by the necessity of detector protection from backgrounds. In the result the beta-function at the final focus quadrupoles can reach 100 km making beam dynamics very sensitive to all kind of errors.

In the present report we consider the effects on momentum acceptance and dynamic aperture of multipole field errors in the body of IR dipoles as well as of fringe-fields in both dipoles and quadrupoles in the case of 1.5 TeV (c.o.m.) MC. Analysis shows these effects to be strong but correctable with dedicated multipole correctors.

Simulations presented in the report are performed using MAD-X code. One of the goals of this study was testing and adaptation of MAD-X code for MC simulations, and also demonstration of the MAD-X code ability to be the “all-in-one” code for MC lattice design and simulations.

¹ Work supported by Fermi Research Alliance, LLC, under contract No.DE-AC02-07CH11359 with the U.S. Department of Energy

CONTENTS

1. Introduction	3
2. Muon Collider Lattice.....	5
2.1. Multipole errors in bending magnets.....	8
2.2. Fringe fields importance for MC.....	9
3. Approaches for simulations of FF and ME with MAD-X.....	11
3.1. Overview of relevant MAD-X modules.	11
3.2. Exporting magnet maps from COSY INFINITY	13
4. Simulation results	15
4.1. Dynamic aperture with fringe fields.....	15
4.2. Chromaticity with multipole errors and its correction.....	16
4.3. Dynamic Aperture with multipole errors.....	20
4.3.1. Sextupolar errors and possible corrections of DA.....	21
4.3.2. DA with decapole errors	25
5. Conclusion.....	26
References	27
Appendix. Calibration of detuning coefficients calculated by PTC_NORMAL and TBT of PTC_TRACK data.	29

1. Introduction

Muon Collider (MC) is presently considered as a possible option for the high energy frontier machine in the post-LHC-era which can be built at FermiLab [1]. To satisfy a number of challenging requirements on the MC lattice, a new approach to the interaction region (IR) chromaticity correction was developed and applied in the design of 1.5 TeV (c.o.m.) MC ring [2-11]. The MC lattice has small beta-functions at interaction point (IP) of order $\beta_{\text{IP}} \sim 1$ cm and is featured by large β -functions and beam sizes at interaction regions (IR) of superconducting (SC) magnets, while the muon beams have relatively large momentum spreads. In this report, specific beam dynamic effects in MC lattice [2-4] designed with this approach are studied.

It is desirable that the IR dipoles have an open mid-plane (OMP) to avoid showering of muon decay electrons in a vicinity of the superconducting coils as well as to reduce background fluxes in the detector central tracker. Preliminary analysis of such dipoles [6, 7] showed that in order to obtain on average good field quality in the region occupied by the beam the relatively large values of higher order geometrical harmonics (or multipole errors) are necessary. Due to large β -functions (maximum values 53 km and 4.4 km) the aperture of IR magnets has to be also large (up to 16 cm), making the fringe-fields potentially detrimental in IR quadrupoles, where beams have large and sharply varying sizes. The relevant details of MC lattice, multipole errors (ME) in OMP dipoles, and a survey on a potential importance of fringe fields in MCs are presented in the section 2.

In this report, we analyze the effect of fringe fields and multipole errors in IR magnets on beam dynamics. Such analysis requires to use adequate simulation tools. The original design and modeling of MC lattice [4-10] has been performed using MAD-8 code [12], which includes a lot of tools for both lattice design and beams dynamics simulations. MAD-8 had been for many years at the forefront of computational physics in the field of particle accelerators design and simulations. Many tasks during MC lattice design have been solved with numerous applications written for the Mathematica package, which provides a high-level interface to MAD-8. Unfortunately, a further development of MAD-8 at CERN has been frozen in 2002. It makes practically impossible any serious modifications and adaptations of MAD-8 for some tasks specific to new rings like a MC.

Since MC lattices had been originally designed with MAD-8, it is naturally to use a similar code preserving the same environments for further analysis. One of the possibilities is to use MAD-X code [12], which is the successor of MAD-8 and which offers most of the MAD-8 functionalities, with some additions, corrections, and extensions including usage libraries of Polymorphic Tracking code (PTC) of E. Forest [13]. Moreover, one of the authors had participated in programming of modern tracking module "PTC-TRACK" being its "module-keeper" for several years. This allows us to adapt and modify this module for MC specific tasks in a testing mode. For these reasons we have accepted MAD-X as an appropriate candidate to be a work horse for further beam dynamics simulations in the MC.

Our usage of MAD-X is aimed at resolution of two specific tasks, which can not be properly resolved on the stage of design and simulations of M.C. ring with MAD-8. These tasks include correct simulations of both the systematic multipole errors in the body of bending magnets and the fringe field effects in magnets located in IR.

PTC modules of MAD-X ensure a proper description for thick magnets utilizing an arbitrary exactness with various symplectic integrators, while high-order multipolar errors are simulated as high-order kicks incorporated into body of thick-magnets. Also PTC modules allows treatments the fringe effects in quadrupoles using so-called "hard-edge" approach. In order to extend abilities for fringe field simulations, the "PTC-TRACK" module has been modified in order to include magnet maps generated by the external code COSY INFINITY [14], which may generate magnet maps taking into consideration realistic shapes of fringe field falloffs. Overview of approaches for simulations of FF and ME with MAD-X are presented in the section 3.

One of the goals for the study presented in this report was a testing and adaptation MAD-X code for MC simulations, and also demonstration of the ability of MAD-X code to be "all-in-one" code for simulations MC lattice designed with MAD-8 code. Therefore, the simulations results presented in the section 4 include also testing simulations with different MAD-X modules. Generally, the results of simulations for the MC lattice show an importance of multipole field errors in the body of IR dipoles as well as of fringe-fields in both dipoles and quadrupoles. Analysis shows these effects to be strong but correctable with dedicated multipole correctors.

2. Muon Collider Lattice

The Table 1 presents the basic parameters of the 1.5 TeV (c.o.m.) MC lattice [2-10]. The lattice design must ensure a large dynamical aperture and momentum acceptance in order to operate with muon beams having relatively large emittances and energy spread.

Table 1. Muon Collider Parameters.

Parameter	Unit	Value
Beam energy	Tev	0.75
IP beta-function, β_{IP}	cm	~ 1
Geom. r.m.s. emittance	nm	6
Momentum acceptance	%	± 0.3
Bending magnetic field in arcs, B	T	$8 \div 10$
Length of quadrupole magnets	m	~ 2
Length of dipole magnets	m	~ 6

The most of critical features of the MC lattice are contained in its interaction region (IR). Figure 1 presents IR layout with locations of correcting magnets and functions related to beta-functions and horizontal dispersion. The special Chromatic Correction Section (CCS) consisting of four sextupole magnets S1, S2, S3, and S4 is inserted in IR region. In order to generate dispersion at the S1 location the first dipole (orange rectangle at the top of Fig. 1) is placed immediately after the final focus doublet which is cut in short pieces to place tungsten masks between them.

The sextupole S1 is located at $\beta_x \approx 0$ and responsible for minimization of the MAD-X vertical chromatic amplitude function W_y . The pair of sextupoles S2 and S4 located at $\beta_y \approx 0$ have the same field strength and are responsible for minimization of the MAD-X horizontal chromatic amplitude function W_x . The sextupole S3 installed between sextupoles S2 and S4 at $\beta_x \approx 0$ is intended for a control of the second order dispersion.

In order to correct high-order chromaticity, the octupole and decapole magnets located at the same places where sexupoles of CCS have been inserted. These correctors are simulated as MAD-X thin multipoles with coefficients k3l and k4l denoting octupole and decapole kicks, respectively.

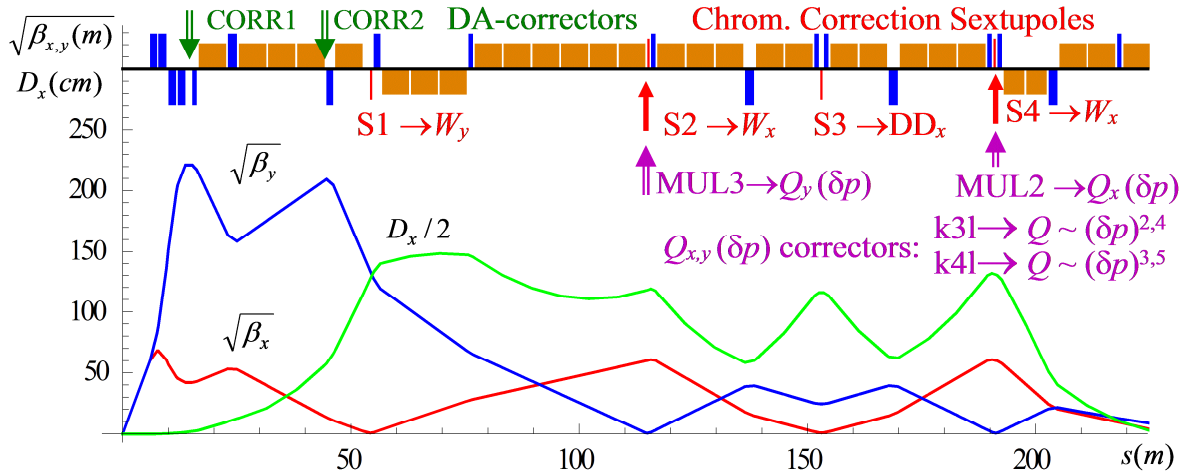


Fig.1 IR optic functions and layout with correctors: chromaticity correction
sextupoles S1-S4 and multipoles MUL1-MUL3,
spherical aberration correctors CORR1 and CORR2.

The MC lattice contains three multipole correctors MUL1, MUL2, and MUL3 located at sextupoles S1, S4, and S3, respectively, while MUL1 is reserved and not used in our simulations. The corrector MUL2 located at S4 with $\beta_y \approx 0$ is used for correction horizontal chromaticity affecting the $Q_x(\delta_p)$ -dependence. The corrector MUL3 located at S3 with $\beta_x \approx 0$ is used for correction vertical chromaticity affecting the $Q_y(\delta_p)$ -dependence. If the $Q(\delta_p)$ -dependencies are considered as polynomial, then the octupole kicks k3l can correct the polynomial coefficients at even powers of δ_p , i.e. δ_p^2 and δ_p^4 , and the decapole kicks k4l can correct the polynomial coefficients at odd powers of δ_p , i.e. δ_p^3 and δ_p^5 .

Two high-order multipoles for corrections of dynamic aperture CORR1 and CORR2 are located in IR near the interaction point (IP) at small values of the horizontal dispersion. These correctors can provide sextupole, octupole, and decapole kicks denoted in MAD-X as k2l, k3l, and k4l coefficients.

The MC lattice prepared with MAD-8 code already contains high-order multipoles used corrections linear and non-linear chromaticities. Let's call this lattice as "original" one. After conversion the MAD-8 MC lattice into MAD-X lattice, the testing particle tracking runs has been performed with MAD "PTC_TRACK" module. Figure 2 shows phase space plots for 4 particles starting at four different values of y -coordinate, $y=6, 12, 18, 24 \mu\text{m}$, and two values of $x=0$ and $6 \mu\text{m}$. These plots demonstrate that the existence of high-

multipoles result in a non-linear behavior of the particle trajectories and non-linear coupling between transverse phase-spaces.

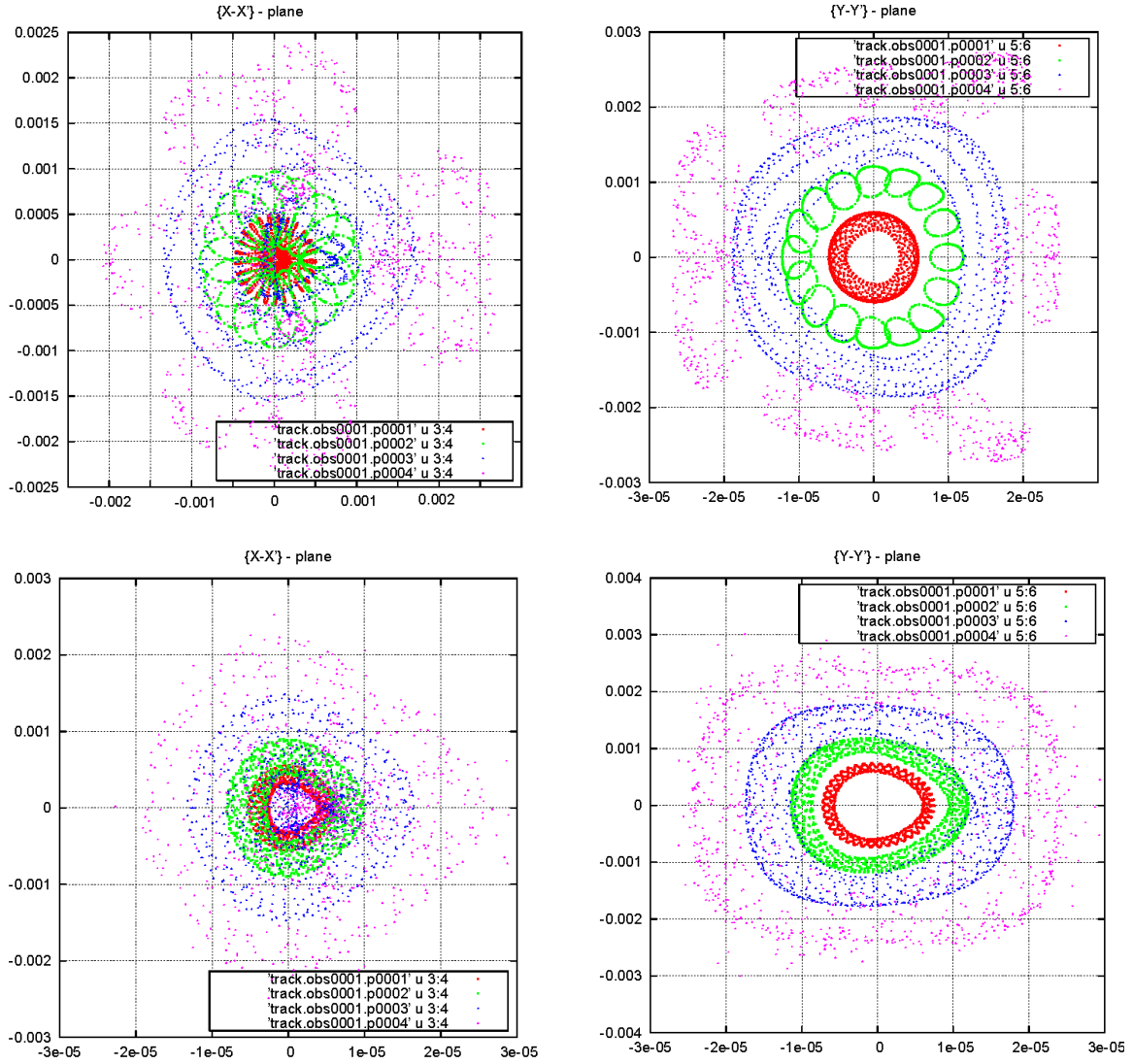


Fig.2 Phase space trajectories on (x, x') and (y, y') planes
at $x=0$ (upper plots) and $x=6 \mu\text{m}$.

2.1. Multipole errors in bending magnets

The IR super-conducting dipoles can be made using the traditional large-aperture $\cos \Theta$ -design, which will require a sufficiently thick inner tungsten liner to protect the cold mass from muon decay product. An alternative is the open-midplane (OMP) design, which allows the decay electrons to pass between the superconducting coils. This design can potentially mitigate problems with heat deposition in the cold mass and detector background fluxes.

The cross-section and good field region of IR dipole coil of OMP-design allowing the passage of the decay electrons are shown in Fig. 3. This magnet configuration provides relatively large values of geometrical harmonics in comparison with the traditional $\cos \Theta$ -design for superconducting magnets.

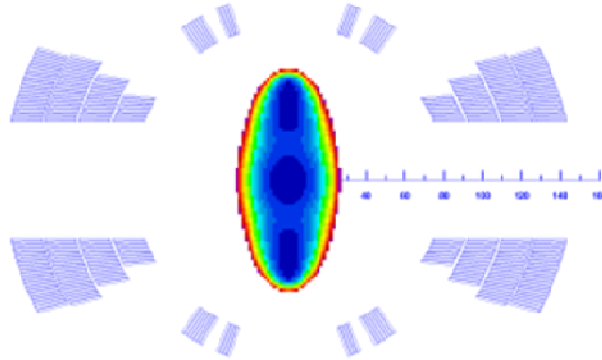


Fig. 3 IR dipole coil cross-section and good field region [6,7].

Geometrical harmonics b_n for IR dipole for $R_{\text{ref}}=40\text{mm}$ presented in Table 2. They are defined by the following standard multipole field expansion:

$$B_y(x, y) + iB_x(x, y) = B_{\text{ref}} \times 10^{-4} \sum_{n=1}^{\infty} (b_n + ia_n) \left(\frac{x + iy}{r_{\text{ref}}} \right)^{n-1}. \quad (1)$$

MAD-code use a different multipole definition given by the following expansion:

$$B_y + iB_x = B\rho \cdot \sum_{m=0}^{\infty} \frac{(k_m^{\text{norm}} + ik_m^{\text{skew}})(x + iy)^m}{m!}, \quad (2)$$

where $m=0, 1, 2$, correspond to the dipole, quadrupole and sextupole fields, respectively.

The multipole orders n and m in the above equations are related by the equation

$m = n - 1$. At the reference field $B_{\text{ref}} = 8$ T and magnetic rigidity $B\rho = 2500$ T·m, the normal multipole coefficients given by the above formulae are related according to the following equation:

$$k_{m=n-1}^{\text{norm}} = 3.2 \cdot 10^{-7} \times \frac{(n-1)!}{r_{\text{ref}}^{n-1}} \cdot b_n. \quad (3)$$

In our simulations with MAD-X code the normal multipole kicks defined as $k_m^{\text{norm}} L$ for the magnet with the length L are used. The values of the k2l, k4l, k6l, k8l, k10l, k12l coefficients in dipole magnets of the length $L = 6$ m are presented in the Table 2. Note, that in the most of our calculation the highest-order multipole kicks k10l, k12l are not used, except the results shown in Fig. 12.

Table 2. Geometrical harmonics b_n at $R_{\text{ref}} = 40$ mm in standard notation and corresponding normal multipole coefficients knl in MAD-code notations.

harmonic #	Value	normal "knl"-kicks	Value
b_3	-5.875	k2l	$-1.41 \cdot 10^{-2}$
b_5	-18.320	k4l	$-3.30 \cdot 10^{+2}$
b_7	-17.105	k6l	$-5.77 \cdot 10^{+6}$
b_9	-4.609	k8l	$-5.44 \cdot 10^{+10}$
b_{11}	0.390	k10l	$+2.59 \cdot 10^{+14}$
b_{13}	0.103	k12l	$+5.65 \cdot 10^{+18}$

2.2. Fringe fields importance for MC

Extensive discussion with a comprehensive list of reference about effects of the fringe fields in accelerator magnets can be found in paper [15]. General tendency is to believe that for the most of rings the fringe field contributions from opposite ends of a magnet cancel each other. This is why the fringe fields of quadrupolar and sextupolar magnets are neglected in the most of tracking codes, e.g. in MAD-8. According to the conclusion of paper [15], the fringe fields effects may be important in some special rings, e.g. in small rings with large emittances and short magnets as the SNS accumulator ring and the muon collider ring. Additional careful considerations should be taken for IR with large variation of the beta-functions. For example, the use of short high-gradient wide-aperture quadrupoles having a short focal length enhance the relevance of their fringe field

effects [16].

Thus, the fringe fields can be important for the MC ring as well due to already mentioned very large β -function values, large magnet aperture and short length of quadrupole pieces (< 2 m). Figure 4 shows vertical and horizontal sizes of the muon beam corresponding to the MC parameters from Table 1. It is empirically adopted that the inner radii of the closest to IP magnets should be larger than about $5\sigma_{\max}$ plus 1 cm. This conditions determines the relatively large aperture radius of the first IR quadrupoles to be equal $a_{Q1}=40$ mm, $a_{Q2}=55$ mm, and $a_{Q3}=80$ mm.

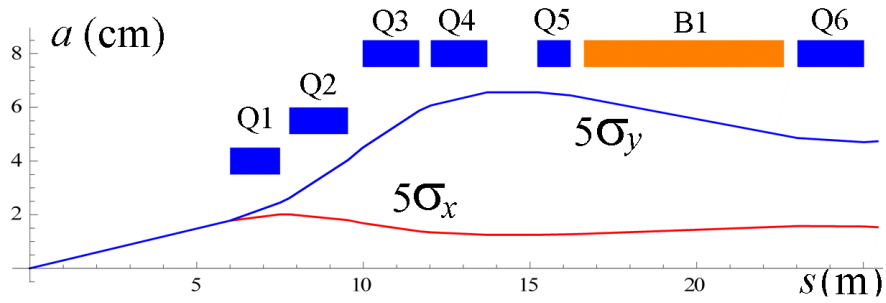


Fig.4 Beam sizes and aperture of the magnets located at IP [6,7].

Starting from 1960th many authors have derived approaches and formulae for treatments of the fringe field effects, e.g. K. Steffen[17], G.E. Lee-Whiting [18], H. Matsuda and H. Wollnik [19], P. Krejcik [20], E. Forest and J. Milutinovic [21] while the most of studies are devoted to the fringe fields in quadrupoles. In the last paper [21], the original Lee-Whiting formulations for the quadrupole fringe effects in the hard-edge limit has been generalized to an explicit symplectic formula including the effects on the time of flight due to δ -dependence. Later these formulae have been implemented in PTC-code [13] and can be called in MAD-X code [12] using PTC-libraries.

The Lee-Whiting formulae take the fringe field effect as a integrated kick neglecting details of field falloffs in the end region. A simple criterion for validity of treating the end region of the length l_{fringe} as short is based on the equality $|\beta'_{x,y}|l_{\text{fringe}} \ll \beta_{x,y}$ [16], where $\beta_{x,y}$ and $\beta'_{x,y}$ are the optical beta-functions and its derivations. With the assumption that the length l_{fringe} is equal to about one aperture diameter, this criterion for IR quadrupoles of considered here M.C. ring is satisfied quite well.

The realistic fringe field falloffs can be simulated in the code COSY INFINITY [14]

using differential algebraic methods. In the paper [22], this code has been used for various studies on fringe field effects. Also some contradictions in the sharp cutoff (or hard-edge) approach are critically discussed, while careful considerations of fringe field effects with account of magnet aperture and falloff shape are recommended. Simulations for an example ring have demonstrated that fringe fields influence on all orders of particle motion, beginning with the linear motion. The fringe fields may affect linear tunes, amplitude dependent tune shifts, chromaticities, and dynamic aperture. The conclusion was that the hard-edge approximation is insufficient and realistic FF falloffs described via the Enge functions should be taken into account.

For these reasons, we have decided to utilize both MAD-X with PTC and COSY INFINITY codes for the fringe field treatments. It might be interesting to compare results with both approach, since the condition for the hard-edge limit $|\beta'_{x,y}|l_{\text{fringe}} \ll \beta_{x,y}$ is well satisfied for considered M.C. ring.

3. Approaches for simulations of FF and ME with MAD-X.

3.1. Overview of relevant MAD-X modules.

Let us consider the MAD-X capabilities for simulation of M.C. lattice taking into account the multipoles errors (ME) and fringe fields (FF). MAD-X consists of two type of modules: a) traditional modules which have the most of MAD-8 functionality; b) PTC modules which provide an interface to PTC library.

Several traditional modules are considered to be relevant for our studies: the Twiss module, THINTRACK module, and SODD module. Twiss module allows calculations of basic optical functions, including Montague chromatic functions, and tunes, chromaticity etc. The module THINTRACK performs particle tracking in the "KICK-DRIFT" lattice converted from original ring lattice with the command MAKETHIN. The SODD module is based on analytical formulae for second order detuning and distortion. These traditional modules allows some artificial treatment of multipole errors in magnets body via splitting a thick magnet into several pieces and inserting multipole kicks between these pieces. Figure 5 shows a simple case of splitting scheme, when one thick magnet is split into pieces.

However, traditional modules ignore any fringe fields of multipole magnets like quadrupole, sextupole, etc. Only linear terms for edge focusing in bending magnets can be simulated. Let us remind that fringe fields of multipolar magnets can not be simulated by thin multipole kicks as multipolar errors in the magnet body. For example, the fringe fields of quadrupole can be regarded as a pseudo-octupole, which can not be replaced by an octupole.

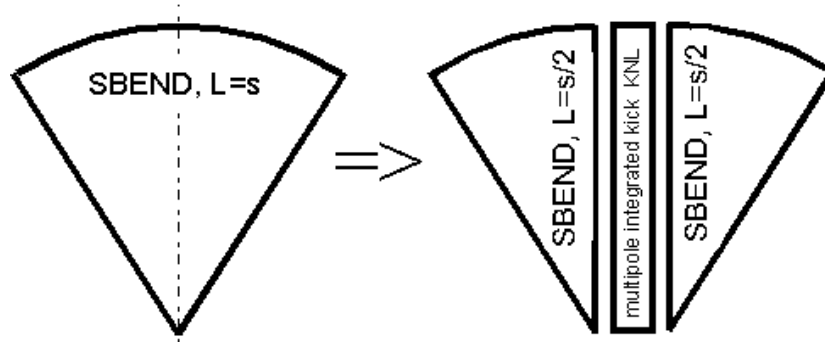


Fig. 5. Splitting scheme for simulations of multipole errors.

Three relevant PTC modules of MAD-X are PTC_TWISS, PTC_TRACK, and PTC_NORMAL. The module PTC_TWISS performs calculations of Ripken optics parameters, but Montague chromatic functions are absent. The module PTC-TRACK performs symplectic tracking in an original thick-magnet lattice and does not require a conversion of the original lattice as THICKTRACK module does. The module PTC_NORMAL uses the PTC normal forms for analysis for calculations non-linear machine parameters: tunes and tune derivatives, dispersion and anharmonicities.

All PTC modules allow natural treatments of high-order multipoles in magnets body via usage of additional options in description of basic magnets. A full range of normal and skew multipole components can be specified in the magnet description as integrated multipole kicks which then are automatically spread over whole thick magnet by PTC according to an applied symplectic integrator. In our simulations multipole errors can be represented as high-order multipoles in bodies of bending magnets. They are described in MAD input script as in the following example:

```
BE1: RBEND, l=0.2, ANGLE=0.1, knl:={0,0,-0.014,0, -330}
```

In the above example among traditional parameters, the parameter `kn1` containing non-zero sextupole and decapole field errors is added.

PTC library can treat the fringe effects in quadrupoles in "hard-edge" approach based on Lee-Whiting formulations [13], if the FRINGE option in PTC library is switched on. In official MAD-X release there is no input commands controlling the FRINGE option, while its default value is off. We have introduced the dedicated switcher in MAD-X input commands to control the state of the FRINGE option in relevant PTC modules.

3.2. Exporting magnet maps from COSY INFINITY

In order to extend our abilities for more detailed and careful fringe field simulations within MAD-X code, the "PTC-TRACK" module has been modified in order to import magnet maps generated for realistic FF falloffs by the external code COSY INFINITY. The importing of several specific types of magnets has been implemented in our simulations, including rectangular dipoles, quadrupoles and sextupoles. The command "FR<mode>" of COSY INFINITY has been used during map generation. The usage of the most precise fringe field mode "FR 3" has been utilized. In this mode the fringe field falloff in a magnet with a full aperture D is based on the standard description of the longitudinal dependence of multiple strength by the Enge function $F = 1/[1 + \exp(P_5)]$ using the fifth order polynomial $P(s)$ depending on normalized longitudinal coordinate $s = z/D$. The polynomial coefficients for a default and simple models given in COSY INFINITY manual have been used in our simulations.

COSY INFINITY allows to calculate maps for total magnet with command "FR 3" and for magnet parts. Maps for magnet body, entrance FF, and exit FF are generated with commands "FR 0", "FR -1", and "FR -2", respectively. The total map can be decomposed as product of entrance, body and exit maps, i.e. $M_{FR3} = M_{FR-1} \circ M_{FR0} \circ M_{FR-2}$. In order to test different possibilities, an import of all four maps has been implemented.

The linear parts of maps generated by COSY INFINITY and MAD-X are different, because the COSY INFINITY generates maps for realistic magnets with finite aperture and finite fringe field falloffs, while MAD codes uses maps for ideal magnets assuming ideal hard-edge field distribution, while neglecting magnet aperture. The linear part of COSY

INFINITY map depends on the shape of fringe fields and magnet diameter, while there are no such dependencies for MAD codes. Due to this fact a simple replacement of MAD element by COSY INFINITY map may results in essential perturbations of linear optics including values of linear tunes.

Moreover it can be stated that MAD code has no elements which can universally substitute even linear part of map generated by COSY INFINITY. The explanation of this fact can be found in Ref. [17, 23], where ideal quadrupoles with hard edge field distribution and real quadrupoles with a bell-shaped field distribution are compared. Let's remind, that the linear transformation matrix for ideal quadrupole is characterized by two parameters, the quadrupole length l_Q and field strength k_Q . The transformation matrix of real quadrupole also can be presented as an "effective" hard edge model. However, the "effective" values of the length l_Q^{eff} and the strength k_Q^{eff} are different for the focusing and defocusing plane. Thus, the linear "effective" hard edge model of real quadrupole is characterized by four parameters l_{QF}^{eff} , k_{QF}^{eff} , and l_{QD}^{eff} , k_{QD}^{eff} .

Our numerical experiments have showed that a direct substitution of COSY maps for quadrupoles results in essential distortion of linear lattice parameters which resulting in drastic effect on high-order beam dynamics, e.g. the dynamic aperture is reduced by many times. Therefore, in order to keep low-order lattice parameters, while investigating high-order effects from realistic fringe fields, we have implemented a possibility to replace the linear parts of imported maps by matrices calculated with hard-edge model. In this case, the stand along fringe fields maps have the unit matrices in linear parts and are denoted as $M_{FR-1}^{[1]}$ and $M_{FR-2}^{[1]}$, and the total and body magnet maps have hard-edge model matrices in the linear parts and are denoted as $M_{FR3}^{[h-edge]}$ and $M_{FR0}^{[h-edge]}$, respectively. However, simple hard-edge model matrices ignore many kinematic effects. In order to keep them, a possibility to combine the imported maps with accurate PTC maps for hard-edge with switched off hard-edge fringe fields $M_{FRINGE=OFF}^{\text{PTC}}$ is also implemented.

After numerical experiments for our MC collider lattice, we have concluded the most preferable combination for the imported map is $M_{FR-1}^{[1]} \circ M_{FRINGE=OFF}^{\text{PTC}} \circ M_{FR-2}^{[1]}$. It allows to preserve a linear lattice parameters with accounting of kinematic effects by PTC maps, while investigating possible manifestation of new effects from realistic fringe fields, which can be sorted out by a comparison of simulation results with reference results obtained with

PTC "hard-edge" fringe fields approach, i.e. with the map $M_{\text{FRINGE=ON}}^{\text{PTC}}$. Note, that the maps import has been implemented only in a development version of MAD-X "PTC-TRACK" module for only element-by-element tracking, and can not be used in other PTC modules.

4. Simulation results

4.1. Dynamic aperture with fringe fields

The effects of fringe fields have been estimated via calculations of dynamic aperture (DA) for the original MC lattice without multipole errors in bodies of the bending magnets. Figure 6 shows simulation results for three different options of the fringe fields simulations in comparison with the lattice without fringe fields. The first option is Lee-Whiting's "hard-edge" fringe field formulation calculated by MAD-X PTC with option FRINGE, which allegedly switched on fringe fields only in quadrupoles. The second option is usage of imported maps only in IR quadrupoles, while the third option use imported maps both in IR quadrupoles and dipoles. The discussed above map scheme $M_{\text{FR-1}}^{[1]} \circ M_{\text{FRINGE=OFF}}^{\text{PTC}} \circ M_{\text{FR-2}}^{[1]}$ is used for both last options.

Figure 6,a shows boundary curves of the stable area on the $(x-y)$ -plane of initial coordinates for particles surviving after 1000 turns. Particles start at IP with zero initial slopes $x' = y' = 0$ and momentum deviations $\delta_p \equiv \Delta p/p = 0$. The fringe field effects results in essential reduction the stability domain, i.e. the value of stable area S_{xy} is reduced by about 45%. Figure 6,b shows dependence of S_{xy} on the relative momentum δ_p .

The curves for all three fringe field options are very close to each other. Similarity of curves for the first and second options confirms our expectations that fringe field regions in our MC lattice can be considered as short and can be treated correctly using the "hard-edge" approach with MAD-X PTC. This similarity indirectly confirms the correctness of our implementation of imported maps. It is also clear that effect of fringe fields in dipoles on dynamical aperture is negligible. Please note that the difference between the results obtained with PTC hard-edge approximation (rose curve) and COSY maps with FF in both quadrupoles and dipoles is quite small and can be explained by tacit inclusion of dipole FF in PTC, not announced in the documentation.

Although effect of fringe fields in quadrupoles is significant, it is not disastrous,

because pseudo-octupole field formed by the fringe fields of quadrupoles can be compensated similar to fields of usual octupole errors.

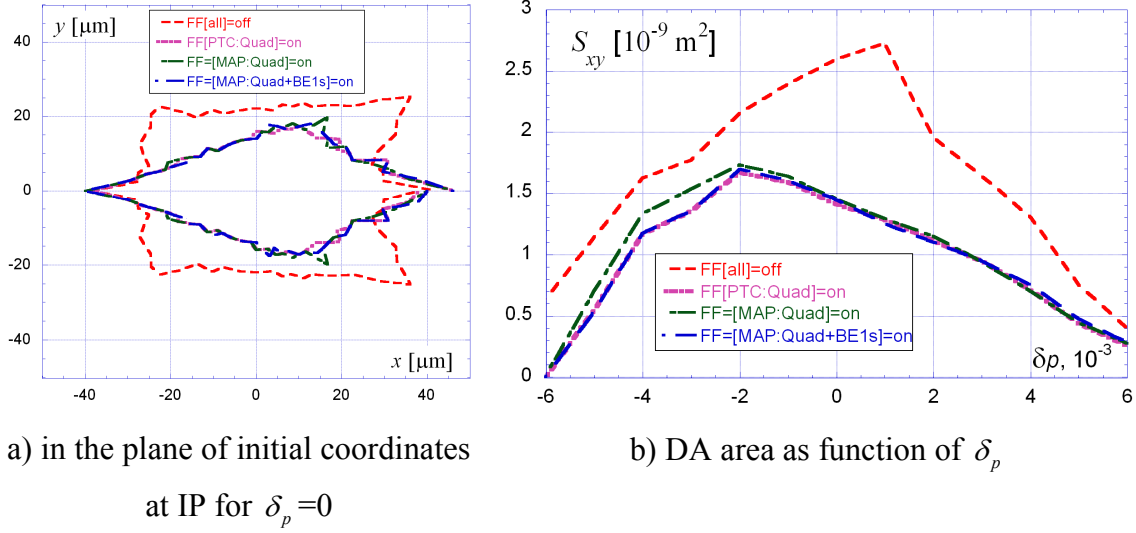


Fig.6 Dynamic aperture for different fringe field models: w/o fringe fields off (red); with PTC fringe fields in quadrupoles (rose); with imported quadrupole maps (green); with imported quadrupole and dipole maps (blue).

4.2. Chromaticity with multipole errors and its correction

The nonlinear chromaticity dependence $Q(\delta_p)$ can be calculated with a traditional MAD-X module TWISS. In this case the multipole errors in the bodies of dipole magnets are simulated using a considered above splitting scheme and fringe fields in quadrupoles are ignored. The lattice preparation using the splitting of the rectangular dipole magnets B1 has been performed in several steps, while controlling and comparing the $Q(\delta_p)$ -dependencies at every step. The steps are the following ones: a) B1 dipoles are originally simulated as MAD-X RBEND; b) RBENDS are replaced by equivalent SBENDS with the entrance and exit pole faces both equal to the half bend angle; c) SBENDS are sliced into five segments; d) five sextupolar kicks k2l simulating multipole errors are inserted in slices. Figure 7 shows $Q(\delta_p)$ -dependencies for these steps. Since the plots for steps *a*, *b*, *c* coincide and overlap each other, Figure 7,a show the plot for the step *a* only.

The sextupole errors in the body of dipole magnets produce large variations in nonlinear $Q(\delta_p)$ -dependencies (see Fig. 7,b), which should be corrected in order to

minimize tune deviations from nominal values within momentum range of $\pm 0.3\%$.

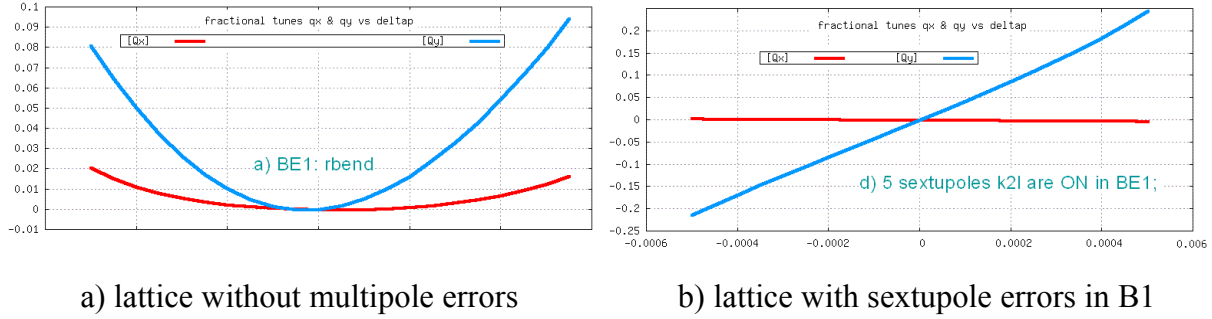


Fig 7 $Q(\delta_p)$ -dependencies calculated with TWISS module.

The TWISS module of MAD-X also allows calculation of Montague chromatic functions in MAD-X formulation. Therefore, all technique used for the linear chromaticity correction with help of chromatic functions in MAD-8 is also available in MAD-X. Figure 8 shows Montague chromatic functions for the MC lattice for steps *a* and *d*. Again since the plots for steps *a*, *b*, *c* overlap each other, only the plot for the step *a* is shown.

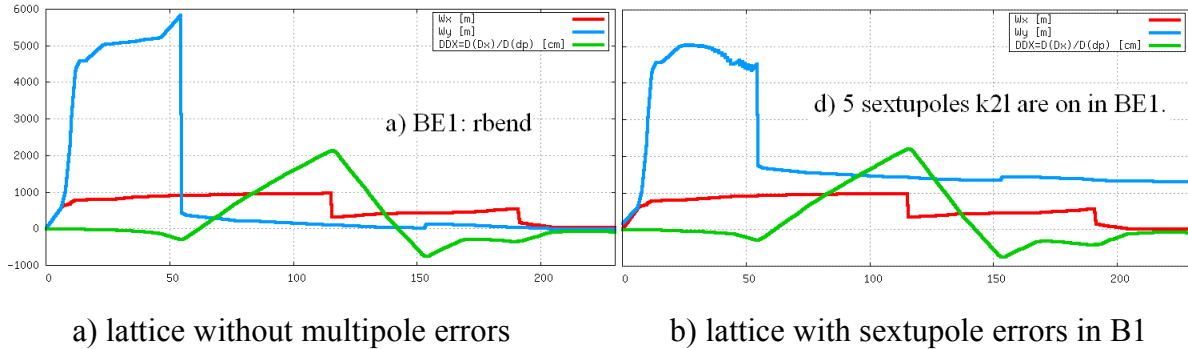


Fig. 8 Montague chromatic functions for the MC lattice

Corrections of the linear chromaticity in the lattice with multipole errors have been performed with matching procedures which use the chromatic functions calculated with TWISS module. Two cases of constraints minimizing the vertical chromatic function W_y have been tested. In the first case, the local constraint setting the zero value of W_y at the specific longitudinal coordinate (the end of sub-line "qring") is applied. In the second case, the constraint is the global zero value of vertical chromaticity along the whole lattice. Both cases of constraints results in the same W_y -curves.

Figure 9,a shows the dependence of the vertical chromatic function W_y on the

longitudinal coordinates for original lattice without multipole errors (red), for the local constraint (blue), and for the global constraint (green). All three W_y -curves coincide quite well. Figure 9,b shows the $Q(\delta_p)$ -dependencies after linear chromaticity corrections. The resulting deviations of tunes after these corrections are even less than in the original lattice. Thus, the corrections of the linear chromaticities with MAD-X can be performed in a manner similar to MAD-8 code.

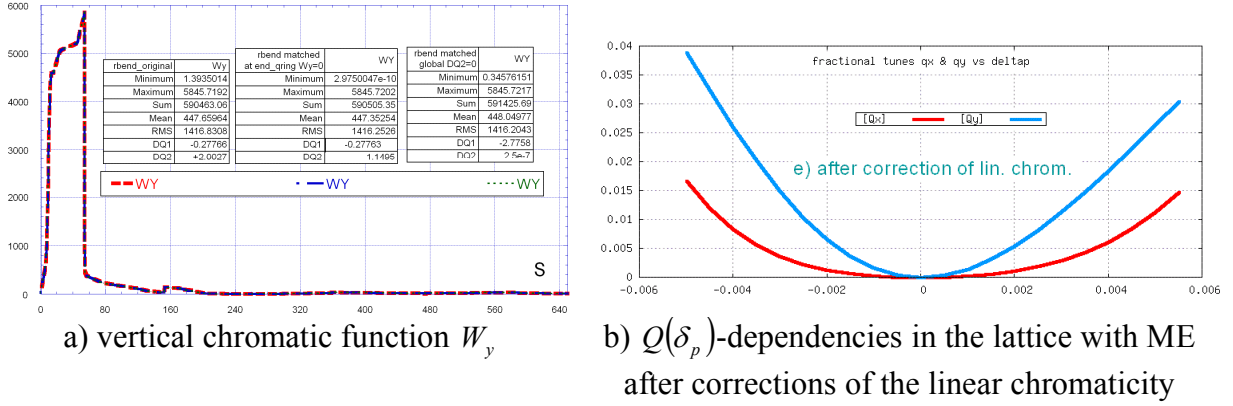


Fig. 9. The correction of linear chromaticity with MAD-X.

The high-order chromaticities can be corrected by variation of octupole and decapole components in multipoles MUL2 and MUL3. The purpose of the correction is minimization of the $Q(\delta_p)$ deviations from nominal value within a given range of momentum deviation δ_p . During the step-by-step minimization procedure it is convenient to present the $Q(\delta_p)$ -curves as polynomial. As discussed above, the octupole components k3l affect the polynomial coefficients at δ_p^2 and δ_p^4 , and the decapole components k4l affect coefficients at δ_p^3 and δ_p^5 . It was helpful to use the plotting software which provides polynomial fitting coefficients. This allows us to see effects from a particular correcting multipole on a particular polynomial coefficient.

Figure 10 shows the final $Q(\delta_p)$ -dependencies for fractional values of $Q_{x,y}$ after corrections of high-order chromaticities in the lattice with multipole errors (see Table 2). The values of polynomial coefficients and correcting multipoles are also shown in the plot.

On the next step, the $Q(\delta_p)$ -dependencies have been tested with PTC_TWISS module. These tests are important, because PTC_TWISS allows us to add simulations of the fringe

field effects in quadrupoles. Figure 11 shows the $Q(\delta_p)$ -dependencies calculated with PTC_TWISS module for the lattice with all multipole errors included, while Figure 11,a show the curves for the same lattice as used for TWISS module.

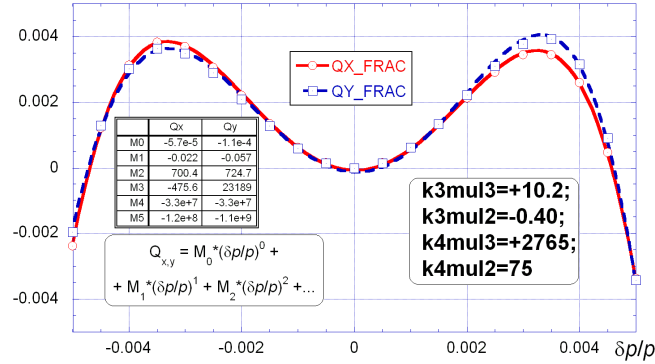


Fig. 10 The corrected $Q(\delta_p)$ -dependencies in the lattice with all multipole errors.

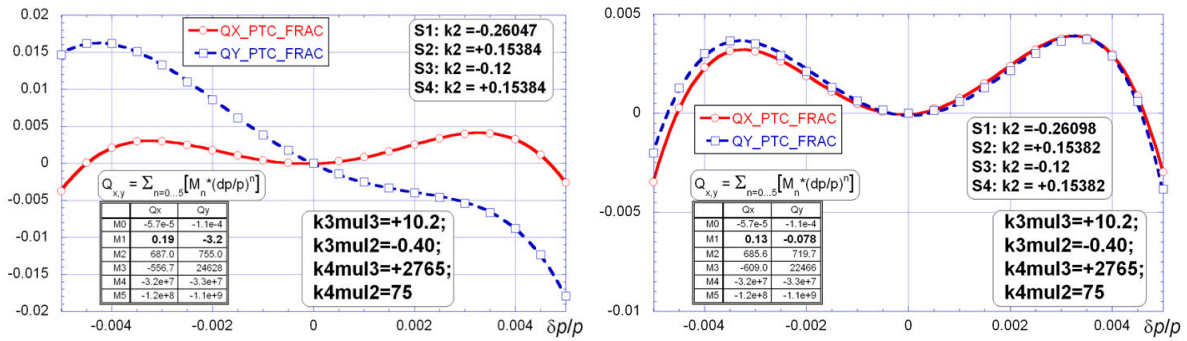


Fig. 11. The $Q(\delta_p)$ -dependencies calculated with PTC_TWISS for the lattice with all multipole errors .

The resulting $Q(\delta_p)$ -curves calculated with TWISS (Fig.10) and PTC_TWISS (Fig.11,a) look are slightly different. PTC_TWISS curves have additional linear slopes. These slopes of PTC_TWISS curves have been corrected with small variations of sextupole correctors S1, S2, S4. The final corrected PTC_TWISS $Q(\delta_p)$ -curves are shown in Figure 11,b. Thus, there is a small difference in the calculated $Q(\delta_p)$ -curves by TWISS and PTC_TWISS modules. This difference can be easily corrected with sextupole correctors.

4.3. Dynamic Aperture with multipole errors

The dynamical aperture has been calculated using particle tracking with PTC_TRACK module in the presence of multipole errors in the bodies of the bending magnets B1. Figure 12 shows effects of multipolar errors in IR dipoles B1 on value of the stable area S_{xy} . The individual (red) and cumulative (blue) effects of multipole errors k2l, k4l, k6l, k8l, k10l, and k12l are presented. By the cumulative effect of e.g. decapole error (k4l) we understand the joint effect of the sextupole and decapole errors with higher multipoles excluded.

Remind again, that results using the highest-order MEs k10l, k12l are presented only for Fig. 12. In all other plots, kicks k10l, k12l are not used due to their negligible effects.

The stable area is most seriously affected by sextupole and decapole errors. The higher multipoles partially compensate their effect but not enough to restore the DA at its original value. Therefore additional correctors are necessary for spherical aberration correction. Two such correctors - CORR1 and CORR2 shown in Fig. 1 – were added to provide sextupole, octupole, and decapole kicks referred to in the following by the MADX coefficient name (k2l, k3l, or k4l respectively). Correction of the effect of sextupole and decapole errors on DA was studied separately.

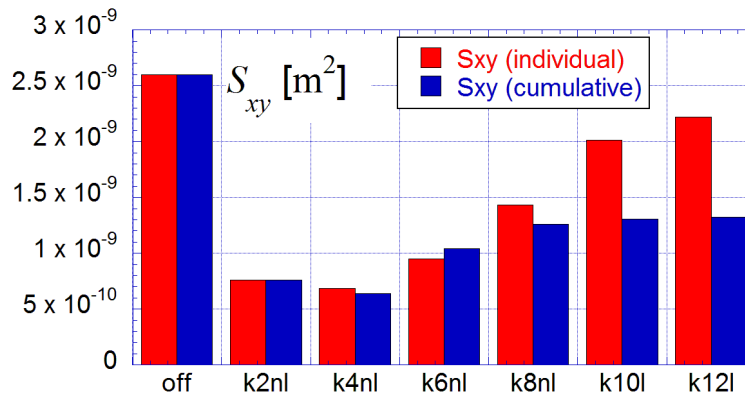


Fig. 12 The stable area S_{xy} at different multipole errors.

4.3.1. Sextupolar errors and possible corrections of DA

Let us use only sextupolar errors in the bodies of dipole magnets B1. Generally, the correction of the errors in order to increase DA can be performed by minimization of so-called detuning coefficients, because an increase in detuning coefficients leads to DA reduction. Detuning coefficients (“tune shifts vs. amplitude”) are helpful for DA optimization. MAD-X offers direct calculations of detuning coefficients with PTC_NORMAL module based on the normal forms. At the first step, we tested detuning coefficients calculated with PTC_NORMAL for our strongly non-linear MC lattice.

The detuning coefficients have been compared with detuning coefficient calculated via particle tracking with PTC_TRACK. In this case, the detuning coefficients, which are derivatives of particle amplitudes, were calculated as finite differences on the mesh defined in the $(x-y)$ -plane with a given step h . The tune values at the mesh nodes were calculated using the turn-by-turn (TBT) analysis of the tracking data. The TBT analysis with efficient algorithms [24] was performed using Mathematica package.

The calculation of detuning coefficients with TBT analysis required to perform a lot of tests in order to choose optimal values for the number of particle turns and the mesh step h . The optimal turn number and the mesh step are found to be equal to 128 and $3\ \mu\text{m}$, respectively. The detailed table with optimization data is presented in the Appendix.

By comparison of the detuning coefficients calculated for our MC lattice with PTC_NORMAL and PTC_TRACK we concluded that only the first order detuning coefficients are consistent. The discrepancies in the second order detuning coefficient do not allow us to consider their values as reliable and their usage in correction procedures should be avoided.

The example for the usage of the first order detuning coefficients for correction of the sextupole errors in the magnet body is presented in Figure 13. The first order detuning coefficients $\partial Q_y / \partial \varepsilon_y$ and $\partial Q_x / \partial \varepsilon_y$ demonstrate a parabolic dependence on the sextupole strength of the corrector CORR1. The optimal value of the sextupole strength minimizing both detuning coefficient is near the cross of two parabolic curves and equals to $k_{2l} = -0.011$.

The TBT analysis of PTC_TRACK data can be also used for finding an optimal strength of the sextupole corrector. Figure 14 shows such an example for corrector CORR1.

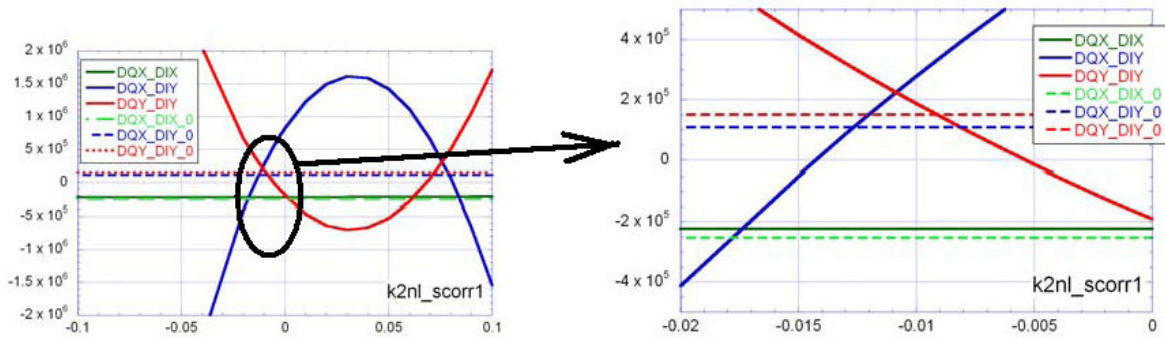


Fig13. PTC_NORMAL detuning coefficients vs the strength of the sextupole corrector CORR1.

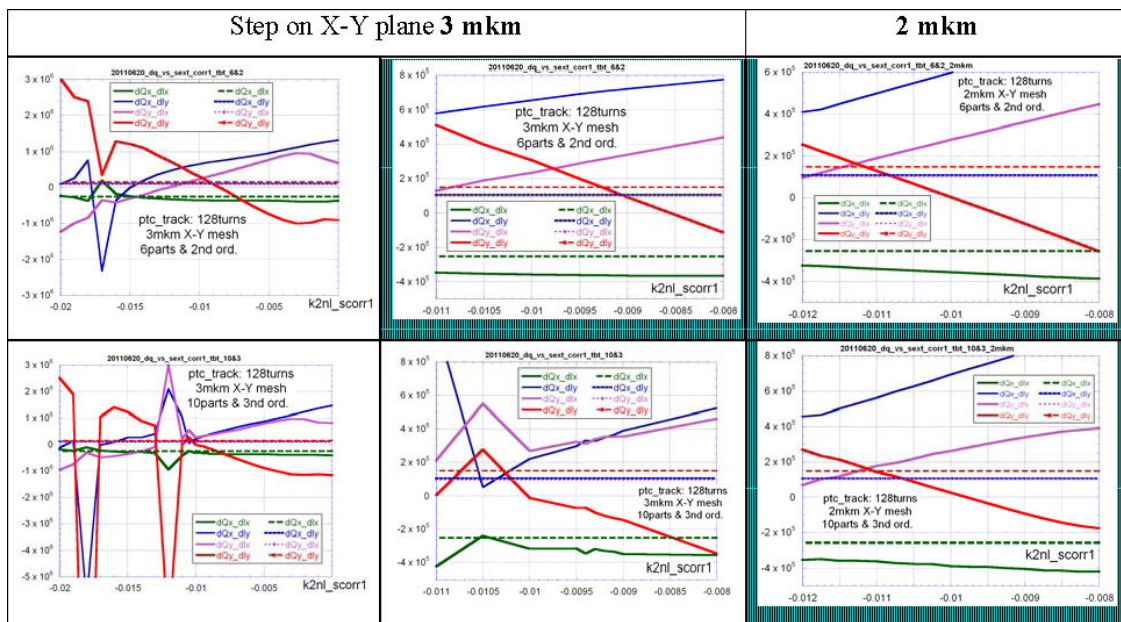


Fig14. TBT with PTC_TRACK detuning coefficients vs the strength of the sextupole corrector CORR1.

The particle tracking over 128 turns has been used. The plots for two mesh steps of 3 μm (left columns) and 2 μm (right column) are presented. The results for two finite difference schemes are shown, the upper plots for an interpolation using 6 node mesh, and the lower plots for interpolation scheme using 10 points. The central column contains magnified images of the left column pictures. The both 6 and 10 node mesh schemes at step of 2 μm provide noiseless curves for $\partial Q_y / \partial \varepsilon_y$ and $\partial Q_x / \partial \varepsilon_y$ curves, but only 6 node mesh scheme provides satisfactory plots for the step value of 2 μm . The optimal values of the sextupole strength are practically the same as with usage of the PTC_NORMAL module.

However, the curves obtained with TBT analysis of PTC_TRACK data are very noisy for the sextupole strength far from the optimal value. This circumstance makes it difficult to use this algorithm for automatic determination of the sextupole correctors optimal strength.

Figure 15 shows the boundary curves on the $(x-y)$ -plane for the three cases: a) the original MC lattice (on the left) without multipole errors; b) the MC lattice with sextupole errors in dipoles B1; c) the MC lattice with sextupole errors in dipoles B1 and sextupole corrector CORR1 with optimal strength of $k_{21}=-0.017$. The values of the areas S_{xy} are also shown on the plot. Using the S_{xy} -values one can conclude that due to sextupole error the stable area is reduced by about 55%, and the sextupole corrector CORR1 can partly increase the S_{xy} -value area, while the final S_{xy} -value is equal to about 70 % of the original lattice. Note, that the S_{xy} -value for the central plot is not consistent with values of the Fig. 12, since the calculations have been performed with slightly different lattice parameters.

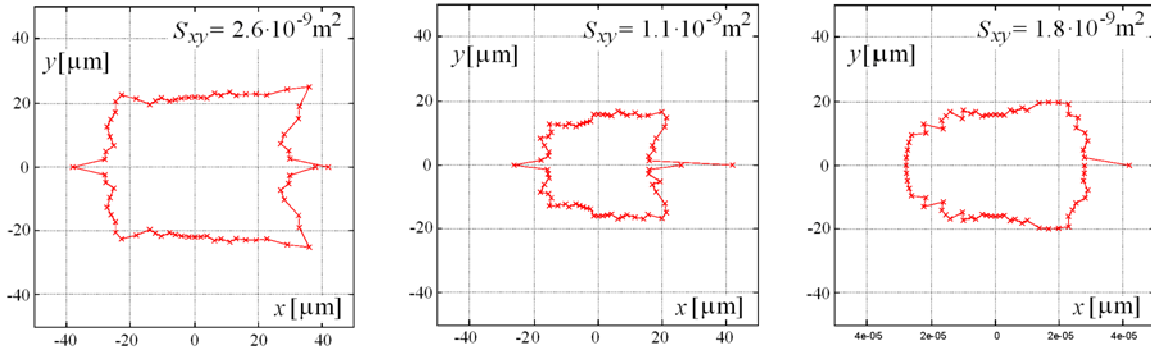


Fig15. Effect of the sextupole errors and sextupole corrector CORR1.

Thus, the usage of PTC_NORMAL is limited to only the first order detuning coefficients, while TBT analysis of PTC_TRACK data requires a lot of preliminary testing. Due to these limitations, one can prefer the straightforward correction procedure based on scanning DA throughout values of the corrector strength. Although such procedure is very time consuming, it may become an universal and powerful tool, if it will be fully automatic.

Figure 16 shows results of the DA scanning for sextupole correctors CORR1 and CORR2. Although the corrector CORR2 is located at non-zero value of horizontal dispersion and may affect the chromaticity, it provides almost full compensation of the S_{xy} -value reduction caused by the sextupole errors.

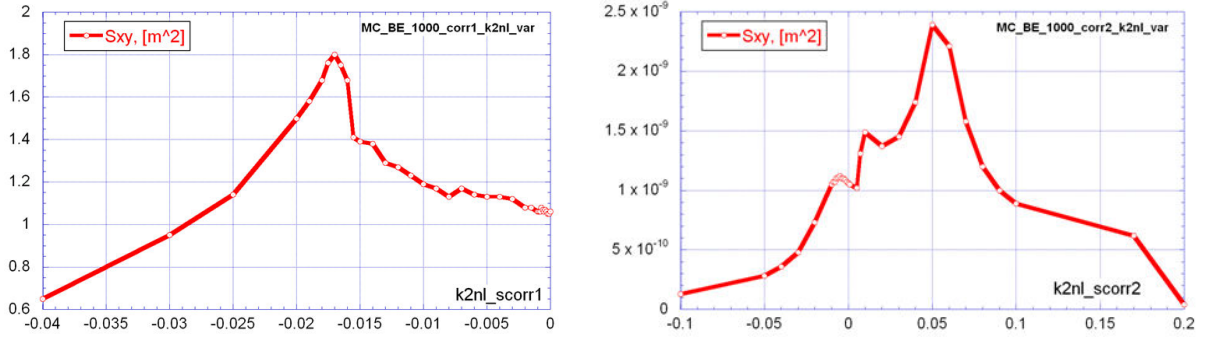


Fig. 16. Scanning of S_{xy} -values for sextupole correctors CORR1 (left) and CORR2 (right).

It is important to have a large dynamic aperture in whole range of the momentum acceptance. For this purposes, DA correction for on-momentum particles should be accompanied by the corrections of non-linear chromaticity within required momentum acceptance. Figure 17 shows the S_{xy} -values vs the constant momentum deviations for three cases: 1) the original MC lattice without multipole errors (red); 2) the MC lattice with sextupole errors in dipole B1 (rose) and corrected with nonlinear chromaticity; 3) the last lattice with switched on sextupole corrector CORR2 (green).

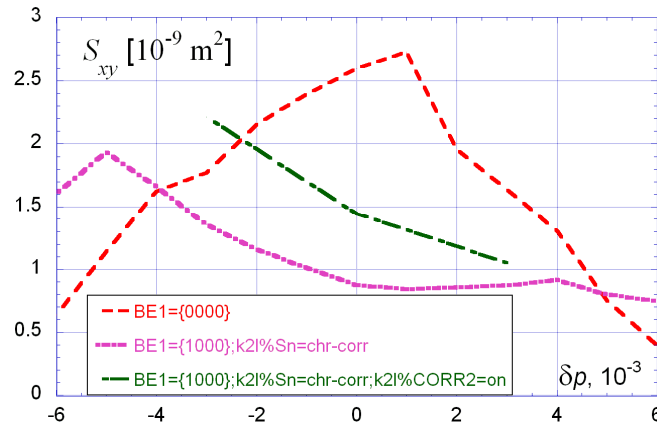


Fig 17. Correction of sextupolar errors within momentum acceptance.

A comparison of the first and second curves demonstrates a possibility of flattening the $S_{xy}(\delta_p)$ -curve in a wide range of momentum deviation. The third curve shows that combination of the sextupole corrector with chromaticity correctors provides a quite flat $S_{xy}(\delta_p)$ -dependence within the momentum acceptance. The boundary curves for on-momentum particles for the cases presented in Fig.17 are shown in Fig.18.

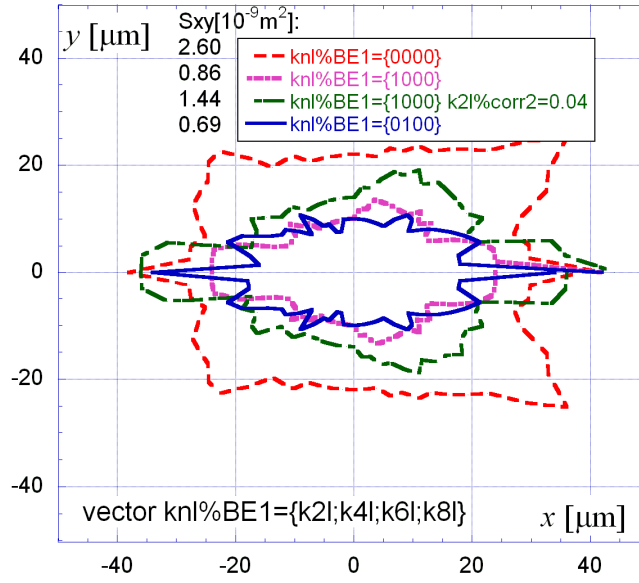


Fig. 18. Stable area on the $(x - y)$ -plane for on-momentum particles.

4.3.2. DA with decapole errors

The early presented Fig. 12 suggests that the decapole errors have the most severe effect of DA. The stable area under action of decapole errors in bodies of dipoles B1 for on-momentum particles is also shown in the above Fig. 18 (blue). Figure 19 shows the $S_{xy}(\delta_p)$ -dependences and the $Q(\delta_p)$ -curves for the lattice affected by decapole errors.

It is seen that DA sharply drops for off-momentum particles. A comparison of the left and right plots of Fig.19 shows that the correction of vertical nonlinear chromaticity does not help. Attempts of scanning S_{xy} -values for on-momentum particles w.r.t. the decapole coefficient in CORR1 and CORR2 does not show any improvement with the strength of decapole correctors. Addition of higher multipole errors given by the kicks **k10l** and **k12l** does not show any effect either. The exact mechanism of the off-momentum DA reduction due to the decapole errors is not determined yet. The observed strong effect of the decapole error is an argument against the open-midplane design making it less attractive. If the open-midplane design will be eventually chosen (for IR dipoles), some space should be reserved for decapole correctors between them.

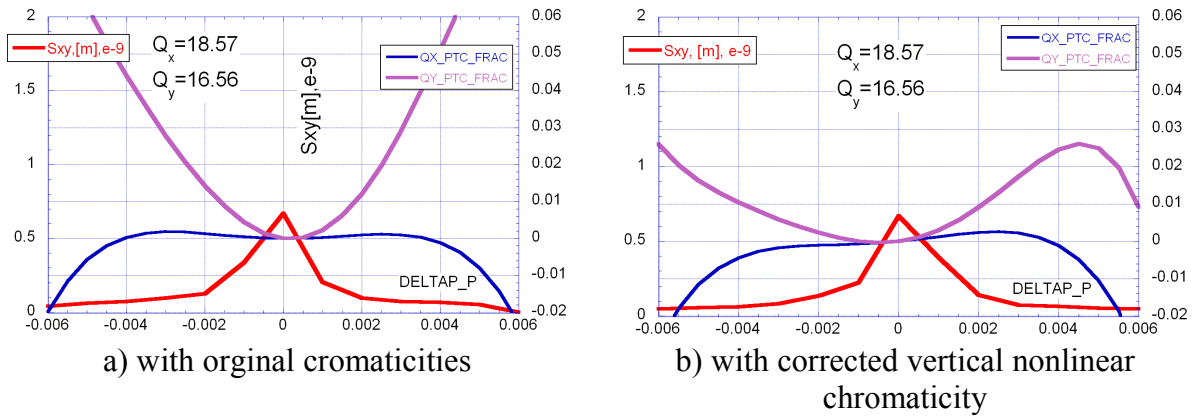


Fig. 19 Decapole effect on off-momentum DA

5. Conclusion

Muon collider (MC) lattice requires simulations with adequate treatments of systematic multipolar errors and fringe fields in quadrupoles. MAD-X code with relevant extensions and modifications can be an appropriate candidate for “all-in-one” code for MC simulations. Combination MAD-X with COSY as a map provider may cover the most of types of quadrupole fringe fields formulations.

Analysis shows that the fringe field errors in quadrupoles can significantly reduce the DA and require correction which we have not attempted yet. The sextupole errors in the body of dipole magnets also reduce DA. This DA reduction can be effectively compensated with a dedicated correctors already included in the design.

The decapole errors in IR dipoles are found to produce the most detrimental effect on dynamic aperture especially for off-momentum particles. If the OMP design will be chosen for IR dipoles, it will be necessary to put additional correctors between them for local correction of decapole errors.

MAD-X modules TWISS, PTC_TWISS and PTC_NORMAL can be used as guiding tools at a design stage, while tracking with PTC_TRACK can provide more reliable results. Some automatization of the DA calculations and TBT analysis of PTC_TRACK data is desirable. It can be done by inclusion into source code both algorithms used in MAD-X input-scripts and external codes like SUSSIX code [25].

References

1. R&D Proposal for National Muon Accelerator Program, FERMILAB-TM-2459-APC (2010).
2. Yu. Alexahin, "Status of the Collider Ring Design", MAP 2012 Winter Meeting at SLAC, 4-8 March 2012².
3. Yu. Alexahin, "Muon Collider Lattice Design Status", workshop "Muon Collider 2011", Telluride CO, June 27-July 1, 2011³ (FNAL, BeamsDB⁴, Beams-doc-3895-v1)
4. Y.I. Alexahin, E. Gianfelice-Wendt, V. Kapin, "Chromaticity Correction for a Muon Collider Optics", Proc. 2011 PAC, New York, 2011, pp. 79-81.
5. Y.I. Alexahin, E. Gianfelice-Wendt, V. Netepenko, "Conceptual Design of the Muon Collider Ring Lattice", IPAC'10, Kyoto, 2010, pp. 1563-1565.
6. Y.I. Alexahin, E. Gianfelice-Wendt, V.V. Kashikin, N.V. Mokhov, A.V. Zlobin, V. Alexakhin, "Muon Collider Interaction Region Design", *ibid.*, pp. 1566-1568.
7. A.V. Zlobin, Y.I. Alexahin, V.V. Kashikin, N.V. Mokhov, "Magnet Design for Muon Collider Ring and Interaction Regions", *ibid.*, pp. 388-390.
8. A. Netepenko, "Muon Collider Lattice Design", FNAL, BeamsDB, Beams-doc-3579-v1, 2010.
9. Yu. Alexahin, "Beam-Beam Effects in Muon Colliders", FNAL, BeamsDB, Beams-doc-3636-v1, 2010.
10. Y.I. Alexahin, E. Gianfelice-Wendt, V. Netepenko, "New Muon Collider lattice design", Beams-doc-3477-v1, 2009.
11. V. Kapin and Yu. Alexahin, "Numerical Simulations of Multipole Errors and Fringe Fields in the 1.5-TeV Muon Collider Lattice Using MADX and COSY codes", talk at APC seminar⁵, Fermilab, 8-Sept-2011.
12. "MAD - Methodical Accelerator Design", versions MAD-X, MAD-9, MAD-8, <http://mad.home.cern.ch/mad/>.

² <https://indico.fnal.gov/conferenceDisplay.py?confId=5097>

³ <https://indico.fnal.gov/getFile.py/access?contribId=63&sessionId=6&resId=0&materialId=slides&confId=4146>

⁴ <http://beamdocs.fnal.gov/AD-public/DocDB/DocumentDatabase>

⁵ <https://indico.fnal.gov/categoryDisplay.py?categId=158>

- 13.E. Forest, F. Schmidt, E. McIntosh, "Introduction to the polymorphic Tracking Code", KEK-Report 2002-3, 2002 .
- 14.M. Berz, "Computational Aspects of Design and Simulation: COSY INFINITY", NIM A-298, p.473, (1990). See also http://bt.pa.msu.edu/index_cosy.htm
- 15.Y. Papaphilippou, J. Wei, R. Talman, "Deflections in magnet fringe fields", Phys. Review E-67, 046502, 2003.
- 16.W. Wan, C. Johnson, J. Holt et al, "The influence of fringe field on particle dynamics in the L.H.C.", Nucl. Instrum. & Meth. in Phys. Res., A-427 (1999), pp.74-78.
- 17.K.Steffen, "High Energy Beam Optics", 1965 by Interscience Publishers.
- 18.G.E. Lee-Whiting, "Third Order Aberrations of a Magnetic Quadrupole Lens", NIM-83, pp.232-244 (1970).
- 19.H. Matsuda, H. Wollnik, "Third Order Transfer Matrices for the Fringing Field of Magnetic and Electrostatic Quadrupole Lenses", NIM-103, pp.117-124 (1972).
- 20.P. Krejcik, Nonlinear Quadrupole End-Field Effects in the CERN Antiproton Accumulators, Proc. PAC, 1987, pp. 1278-1280.
- 21.E. Forest and J. Milutinovic, Leading Order Hard Edge Fringe Fields Effects in $(1+\delta)$ and Consistent with Maxwell's Equations for Rectilinear Magnets, NIM A-269, pp.474-482 (1988).
- 22.M. Berz, B. Erdelyi, and K. Makino, "Fringe field effects in small rings of large acceptance", Phys. Rev. ST-AB, Vol. 3, 124001 (2000).
- 23.H.Wiedemann, "Particle Accelerator Physics", 3rd edition, 2007 by Springer-Verlag, pp. 125-128.
- 24.R. Bartolini, M. Giovannozzi, W. Scandale, A. Bazzani, E. Todesco, "Algorithms for a Precise determination of the betatron tune", Proc 1996 EPAC, pp. 1329.
- 25.R. Bartolimi, F. Schmidt, "SUSSUX: A Computer Code for Frequency Analysis of Non-linear Betatron Motion", CERN SL/Note 98-017 (AP) updated Jan-2005.

Appendix. Calibration of detuning coefficients calculated by PTC_NORMAL and TBT of PTC_TRACK data.

Parameter	ptc norm	track 2^10 (1024) (tbt: 1/N/2)	Netepenko
nst, no (N-forms)	10 (-as1), exact, no=5,6	nst=1, exact uniform mesh on X-Y plane "10-2ord//6-2ord" points or ".../10-3ord"	
Nturns		64	128
step on (X-Y)		256	512
		h=3mkm	1024
		w/o l-aver	with l-aver
qx	by twiss	5599935/18.560000	5599973/18.560000
		5600039/0.56	5600007/0.56
		5600043/0.56	5600008/0.56
qy	by twiss	5500534/18.550000	5499953/18.550000
		5499969/0.55	5500032/0.55
	by ptc-normal	5499945/0.55	5500035/0.55
$\partial Q_x / \partial \varepsilon_x$	-2.63e05	-2.6/-2.6/-2.5 E5	-2.5/-2.5/-2.5 E5
$\partial Q_x / \partial \varepsilon_y$	1.27e5	+6.7/+3.9/+3.5 E4	+1.2/+1.1/+1.1 E5
$\partial Q_y / \partial \varepsilon_x$	1.27e5	-9.9/+2.5/-5.0 E4	+1.2/+1.0/+1.0 E5
$\partial Q_y / \partial \varepsilon_y$	-2.39e5	+1.4/+1.5/+1.5 E5	+1.5/+1.5/+1.5 E5
$\partial^2 Q_x / \partial \varepsilon_x^2$	-6.68e10	+2.1/+0.4/+0.02 E12	+0.1/+0.8/+1.4 E13
$\partial^2 Q_x / (\partial \varepsilon_x \partial \varepsilon_y)$	4.97e14	-6.0/-6.6/-8.3 E12	+0.9/+1.8/+2.5 E13
$\partial^2 Q_x / \partial \varepsilon_y^2$	-5.05e14	-3.4/-2.4/-1.7 E13	-1.7/-1.2/-0.9 E13
$\partial^2 Q_y / \partial \varepsilon_x^2$	4.97e14	+2.8/-2.0/-6.0 E13	+1.7/+1.4/+1.1 E13
$\partial^2 Q_y / (\partial \varepsilon_x \partial \varepsilon_y)$	-5.05e14	-1.2/-2.0/-2.1 E13	-1.8/-1.6/-0.1 E13
$\partial^2 Q_y / \partial \varepsilon_y^2$	-1.61e12	-1.3/-1.1/-0.8 E12	-2.6/-3.2/-1.9 E12